

## Supplementary Information

### **Charting the relationship between the phase type-surface area-interactions between the constituent atoms and oxygen reduction activity of Pd-Cu nanocatalysts inside fuel cells by *in operando* high-energy x-ray diffraction**

Yazan Maswadeh,<sup>a</sup> Shiyao Shan,<sup>b</sup> Binay Prasai,<sup>a</sup> Yinguang Zhao,<sup>b</sup> Zhihui Xie,<sup>b</sup> Zhipeng Wu,<sup>b</sup> Jin Luo,<sup>b</sup> Yang Ren,<sup>c</sup> Chuan Jian Zhong,<sup>b</sup> and Valeri Petkov<sup>a</sup>

<sup>a</sup>Department of Physics, Central Michigan University, Mt. Pleasant, Michigan 48859, United States

<sup>b</sup>Department of Chemistry, State University of New York at Binghamton, Binghamton, New York 13902, United States

<sup>c</sup>X-ray Science Division, Advanced Photon Source, Argonne National Laboratory, Argonne, Illinois 60439, United States

#### 1. Sample preparation

Pd-Cu alloy nanoparticles (NPs) were synthesized following a procedure reported in refs.<sup>S1-S4</sup>. Briefly, palladium (II) acetate ( $\text{Pd}(\text{OCOCH}_3)_2$ ) and copper (II) acetate ( $\text{Cu}(\text{OCOCH}_3)_2$ ) were mixed in a desired ratio into ethylene glycol solvent. The solution was stirred vigorously under  $\text{N}_2$  atmosphere for 10 mins. Oleic acid and oleylamine were added into the solution and used as capping agents. 1,2-hexadecanediol was also added and used as a reducing agent. Temperature was then increased slowly to 120 °C until the metal precursors started to decompose and the solution turned dark. The mixture was further heated up to 200 °C with reflux for 0.5 hr followed by cooling down to room temperature. The resulting NPs were precipitated out by adding ethanol followed by settling for 12 hours. Finally, the NPs were dried under  $\text{N}_2$  atmosphere and re-dispersed in hexane solvent for further use. Note, in comparison with the synthesis protocol adopted in our earlier work<sup>S3</sup>, longer reaction and digesting time were used here.

The so-synthesized Pd-Cu NPs were deposited on carbon black (Ketjen) through suspending 200 mg of it in 20 mL hexane containing ~80 mg nanoparticles and stirring for ~15 hours. The resulting powder was collected and dried under  $\text{N}_2$  atmosphere. Carbon supported NPs were activated for catalytic applications by heating at 260 °C in  $\text{N}_2$  for 30 min followed by heating at 400 °C in 15 vol. %  $\text{H}_2$  for 120 min. The loading of the Pd-Cu NPs on the carbon supported catalysts was determined by thermal gravimetric analysis and found to be about 40 wt. %.

ii) Studies on the ORR activity of Pd-Cu alloy under actual operating conditions

Membrane electrode assemblies (MEAs) were prepared using fresh Pd-Cu alloy NPs as a PEMFC cathode (ORR) catalyst and commercial Pt NPs (E-tek) as a PEMFC anode (hydrogen oxidation reaction) catalyst. In particular, the respective (carbon-supported) metallic NPs were dissolved in 5 wt% Nafion-containing solution as to achieve NP concentration of 2-3 mg/mL. The catalyst-Nafion solution (ink) was brush coated on wet-proof carbon paper (Spectracarb 2050A-0550). The anode and cathode catalyst coated carbon paper was fused to the respective sides of a Nafion membrane (Nafion 212 membrane, DuPont) by hot pressing at 120 °C. The resulting sandwich-type {Carbon Paper-Anode Catalyst-Nafion Membrane-Cathode Catalyst-Carbon Paper} assembly was transferred to the custom-made PEMFC shown in Figure S3. The PEMFC was cycled between 0.6 to 1.2 V following a protocol recommended by DOE<sup>S5</sup>. During the cycling, high purity hydrogen gas (3.5% H<sub>2</sub> balanced by He) was fed to the PEMFC anode compartment at a rate of 50 mL/min. Before reaching the anode, the gas was forced through a water bubbler to achieve 100 % humidity. High-purity nitrogen gas was flown through the PEMFC cathode compartment. The current output of the PEMFC was recorded during the voltage cycling which lasted for about 8 h (~1500 cycles). Selected polarization curves showing the current output of the PEMFC resulted from the repetitive application of external voltages are shown in Figure 1. The full set of polarization curves is summarized in Figure S15. The curves are typical for catalysts subjected to accelerated tests for ORR activity and stability (e.g. see Figure 2 in refs. [S6]).

iii) Atomic PDFs derivation and interpretation

Experimental HE-XRD patterns for Pd-Cu alloy NPs were corrected for experimental artifacts, in particular for the strong background-type scattering originating from the PEMFC hardware (see Figure S16), and then used to derive the so-called total structure factors defined as:

$$S(q) = 1 + \left[ I^{coh.}(q) - \sum c_i |f_i(q)|^2 \right] / \left[ \sum c_i f_i(q) \right]^2, \quad (S1)$$

where  $I^{coh.}(q)$  are the coherently scattered intensities extracted from the raw HE-XRD patterns,  $c_i$  and  $f_i(q)$  are the concentration and x-ray scattering factor, respectively, for atomic species of type

$i$  ( $i$ =Pd and Cu). The structure factors were Fourier transformed into the so-called total atomic PDFs,  $G(r)$ , as follows:

$$G(r) = \frac{2}{\pi} \int_{q=0}^{q_{\max}} q[S(q) - 1] \sin(qr) dq, \quad (\text{S2})$$

where  $q$  is the magnitude of the wave vector ( $q=4\pi\sin\theta/\lambda$ ),  $2\theta$  is the angle between the incoming and outgoing x-rays,  $\lambda$  is the wavelength of the x-rays used,  $r$  is the radial (real space) distance and  $q_{\max}$  extends to  $25 \text{ \AA}^{-1}$ . Experimental *in operando* HE-XRD patterns and the respective atomic PDFs are summarized in Figure 1. Note, Fourier transformation is a unitary operation and so does not alter in any way the atomic-structure relevant information contained in HE-XRD data.

As defined, the total atomic PDF  $G(r) = 4\pi r[\rho(r) - \rho_0]$ , where  $\rho(r)$  and  $\rho_0$  are the local and average atomic number density of Pd-Cu alloy NPs. Hence, the PDF  $G(r)$  peaks at real space distances separating Pd and Cu atoms, immediate and all farther neighbors, within the NPs studied. The area of the peaks is proportional to the number of Pd-Pd, Pd-Cu and Cu-Cu atomic pairs at those distances. Accordingly, each of the *in operando* atomic PDFs shown in Figure 1 is a weighted sum of 3 partial atomic PDFs  $G_{ij}(r)$ , in particular  $G_{\text{Pd-Pd}}(r)$ ,  $G_{\text{Pd-Cu}}(r)$  and  $G_{\text{Cu-Cu}}(r)$  partial PDFs<sup>S7-S9</sup>, that is:

$$G(r) = \sum_{i,j} w_{ij} G_{ij}(r), \quad (\text{S3}).$$

Here  $w_{ij}$  are weighting factors depending on the x-ray scattering power,  $f_i(q)$ , and the concentration,  $c_i$ , of Pd and Au species in the respective Au-Pd alloy NPs as follows:

$$w_{ij} = c_i c_j f_i(q) f_j(q) / [\sum c_i f_i(q)]^2 \quad (\text{S4}).$$

Though, since Pd atoms ( $Z=46$ ) scatter x-rays much stronger than Cu atoms ( $Z=29$ ), the *in operando* atomic PDFs obtained here are indeed much more sensitive to atomic pairs involving Pd than Cu atoms alone.

Another important point is to made here: Since surface atoms at the opposite sides of NPs are separated the most, experimental  $G(r)$ s would show distinct peaks *only* up to distances close to the average size of the particular NPs studied, as demonstrated in Figure S4. As can also be seen in the Figure, PDF peaks at the higher- $r$  distances would largely reflect pairs of atoms close to the NP surface. Hence, experimental atomic PDFs are sensitive to the atomic-scale structure throughout metallic NPs, including the NP surface whereat chemical reactions take place. This

fact may not come as a surprise since atoms at the surface of metallic NPs used in catalysis (typically < 15 nm) occupy a substantial fraction of the overall volume of the NPs, and HE-XRD is known to be sensitive to the volume fraction of the constituents of a metallic material down to a few %<sup>S10</sup>. For reference, atoms in the top two layers of Pd-Cu alloy NPs studied here are about 25 % of all atoms in the NPs.

iv) Generating of 3D model nanophases for Pd-Cu alloy NPs by Molecular Dynamics

3D models featuring plausible nanophase types for Pd-Cu alloy NPs were built by Molecular Dynamics (MD) simulations based on the quantum corrected Sutton-Chen (SC) method<sup>S11-S14</sup>. In brief, the method considers atomic pair interactions in metals and alloys as a sum of two constituents. One accounts for the repulsion between metal atom cores and the other - for the attractive force between metal atom cores due to the electrons surrounding the cores. Accordingly, the energy of atomic-level models,  $U$ , appears as a sum of an atomic pair potential  $V(r_{ij})$  term and a local electron density ( $\rho_i$ ) term defined as follows:

$$U = \sum_i \left[ \sum_{j \neq i} \frac{1}{2} h_i \epsilon_{ij} V(r_{ij}) - c_i \epsilon_{ij} (\rho_i)^{\frac{1}{2}} \right] \quad (\text{S5})$$

where

$$V(r_{ij}) = \left( \frac{a_{ij}}{r_{ij}} \right)^{n_{ij}} \quad \text{and} \quad \rho_i = \sum_{j \neq i} \left( \frac{a_{ij}}{r_{ij}} \right)^{m_{ij}} \quad (\text{S6}).$$

The so-called “energy” parameter  $\epsilon_{ij}(meV)$  and the dimensionless parameter  $c_i$  are used to scale appropriately the interatomic repulsive  $V(r_{ij})$  and attractive ( $\rho_i$ ) metal-to-metal atom interactions, respectively. Parameters  $m_{ij}$  and  $n_{ij}$  are positive integers such that  $n_{ij} < m_{ij}$ . The parameter  $a_{ij}$  is a quantity used to scale appropriately distances  $r_{ij}$  between  $i$  and  $j$  type atoms in the structure models. SC parameters for Pd and Cu were taken from literature sources<sup>S12,S13</sup>. The interactions between unlike atoms, i.e.  $i$ - $j$  type atomic interactions, were estimated by a mixing rule described in Ref. [S14].

Since, in general, the realism of MD simulations is dependent both on the structure models chosen and conditions under which the simulations are run, the initial model atomic configurations considered here reflected the average size (5.1 – 5.9 nm), shape (spherical) and chemical composition of Pd-Cu NPs modeled. The configurations featured fcc Pd-Cu alloy NPs,

fcc Pd-Cu alloy NPs with a surface enriched in Pd, Janus-type Pd-Cu NPs, fcc Pd-Cu NPs with a surface enriched in Cu, bcc Pd-Cu alloy NPs, pure Cu core-Pd shell NPs, pure Pd core-Cu shell NPs, Pd-Cu-Pd sandwich type NPs and NPs whose inner and outer portion are formed of a bcc Pd-Cu alloy and fcc Pd-Cu alloy rich in Pd, respectively. The configurations were optimized in terms of energy, i.e. stabilized at atomic level, with the help of the computer program DL-POLY<sup>S15</sup>. The optimization was performed under canonical NVT ensemble in the absence of periodic boundary conditions. Velocity Verlet algorithm with a time step of 2 fs was used.

Typically, MD simulations on metallic systems involve quenching of atomic configurations equilibrated at very high temperature (often above melting temperature). However, as it is the common practice in nanocatalysis, Pd-Cu NPs were synthesized in solution at room temperature and then subjected to a post-synthesis treatment at 400 °C, i.e. they were not obtained by rapid quenching from a melt. Hence, the initial atomic configurations used in the MD simulations were not melted but equilibrated for 200 ps at 400 °C, cooled down to room temperature in steps of 50 K and again equilibrated for 100 ps. The resulting 3D nanophase models for Pd<sub>x</sub>Cu<sub>100-x</sub> alloy NPs ( $x = 34, 51, 75$ ) with an average size of 6 nm are shown in Figures S8, S9 and S10, respectively. Altogether, the models are with a realistic size, shape and chemical composition. Furthermore, the models are optimized in terms of energy. As such, they provide a realistic basis for determining the nanophase type of Pd-Cu alloy NPs through comparing experimental and model computed atomic PDFs.

#### *iv) Nanophase analysis of Pd-Cu alloy NPs*

The nanophase type of fresh and cycled Pd<sub>x</sub>Cu<sub>100-x</sub> alloy NPs ( $x = 34, 51, 75$ ) was determined by a procedure involving matching atomic PDFs derived from the MD built model nanophases against the respective experimental PDFs. A model reproducing the experimental data in very good detail, i.e. minimizing the residual between the model computed and experimental PDF, is considered a truthful representation of the nanophase type of the respective NPs. In particular, as exemplified in Figure S11, a comparison between atomic PDFs computed from model nanophases with a chemical composition of Pd<sub>3</sub>Cu<sub>1</sub> and the experimental PDF for Pd<sub>75</sub>Cu<sub>25</sub> NPs undergone 1450 PEMFC cycles reveals that the NPs are an fcc Pd-Cu alloy whose surface is enriched in Pd. Applying the procedure, we found that the core and shell of Pd<sub>34</sub>Cu<sub>66</sub> and Pd<sub>51</sub>Cu<sub>49</sub> NPs are a bcc Pd-Cu and fcc Pd-Cu alloy, respectively. Besides, the shell (near-surface

region) of both NPs is enriched in Pd. The results of nanophase analysis are unambiguous because, as shown in Figure 2b, fcc Pd-Cu alloy nanophase rich in Pd at the surface and bcc Pd-Cu alloy core @ fcc Pd-Cu shell nanophase rich in Pd, i.e. cycled Pd<sub>34</sub>Cu<sub>66</sub> and Pd<sub>25</sub>Cu<sub>75</sub> NPs, respectively, produce significantly different atomic PDFs.

Once determined, the nanophase type of Pd<sub>x</sub>Cu<sub>100-x</sub> alloy NPs ( $x = 34, 51, 75$ ) was explored as a function of the number of PEMFC cycles. For the purpose, the occupancy of particular atomic positions in the respective 3D nanophase model were adjusted, e.g. Cu atoms near the model's surface were replaced by Pd atoms, so that the model-derived atomic PDF reproduced the respective *in operando* atomic PDF in good detail. As demonstrated in Figure 2a, the latter are sensitive to changes in the ratio of Pd and Cu atoms in the NPs occurring during the PEMFC operation. The exploration was facilitated by the fact that the chemical composition of fresh and cycled (1450 times) Pd-Cu alloy NPs was known thanks to the independent ICP-AES experiments conducted here. As data in Figures S12, S13 and S14 exemplify, largely, Pd<sub>x</sub>Cu<sub>100-x</sub> alloy NPs ( $x = 34, 51, 75$ ) preserve their nanophase type during cycling. Structural characteristics of the NPs such as atomic pair (bonding) distances and the relative nanophase composition, i.e. the volume ratio of the bcc core and fcc shell, though, change significantly during the PEMFC operation. The changes are summarized in Figures 3, 4 and 5, respectively.

The MD built models are also easy to adjust as to reflect changes in the size of Pd-Cu alloy NPs occurring during the PEMFC operation. For example, by removing a fraction of the top surface layer of the 3D nanophase models shown in Figures S8, S9 and S10, the size of the models can be reduced from 6 nm to about 5.2 nm. It is to be underlined here that determining the phase type of materials through comparing experimental diffraction data with data for reference phases, known as “phase-analysis”, is a widely applied technique in materials research and technology<sup>S10</sup>.

## REFERENCES:

- S1. J. Yin, S. Shan, M. S. Ng, L. F. Yang, D. Mott, W. Fang, N. Kang, J. Luo and C. J. Zhong, *Langmuir*, 2013, **29**, 9249.
- S2. Z. Yin, W. Zhou, Y. J. Gao, D. Ma, C. Kiely and X. H. Bao, *Chem-Eur J.*, 2012, **18**, 4887.
- S3. S. Shan, V. Petkov, B. Prasai, J. F. Wu, P. Joseph, Z. Skeete, E. Kim, D. Mott, O. Malis, J. Luo and C. J. Zhong, *Nanoscale*, 2015, **7**, 18936.
- S4. J. F. Wu, S. Shan, J. Luo, P. Joseph, V. Petkov and C. J. Zhong, *ACS Appl. Mater. Inter.*, 2015, **7**, 25906.

- S5. R. Borup, J. Meyers, B. Pivovar, Y. S. Kim, R. Mukundan, N. Garland, D. Myers, M. Wilson, F. Garzon, David Wood, P. Zelenay, K. More, K. Stroh, T. Zawodzinski, J. Boncella, J. E. McGrath, M. Inaba, K. Miyatake, M. Hori, K. Ota, Z. Ogumi, S. Miyata, A. Nishikata, Z. Siroma, *Chem. Rev.*, 2007, **107**, 3904.
- S6. C. A. Rice, Patrick Urchaga, A. O. Pistono, B.W. McFerrin, B. T. McComb and J. Hu, *J. Electrochem. Soc.*, 2015, **162**, F1175.
- S7. Y. Waseda in *Anomalous X-Ray Scattering for Materials Characterization: Atomic-Scale Structure Determination*. (Springer: Berlin, 2002).
- S8. V. Petkov and S. D. Shastri., *Phys. Rev. B*, 2010, **81**, 165428.
- S9. C. Wurden, K. Page, L. Llobet, C. E. White and Th. Proffen., *J. Appl. Crystallogr.*, 2010, **43**, 635.
- S10. P. K. Klug and L. E. Alexander in “*X-Ray Diffraction Procedures: For Polycrystalline and Amorphous Materials*” (Wiley, 1974).
- S11. M. W. Finnis and J. E. Sinclair, *Philos. Mag. A*, 1984, **50**, 45.
- S12. A. P. Sutton and J. Chen, *Philos. Mag. Lett.*, 1990, **61**, 139.
- S13. Y. Kimura, Y. Qi, T. Cagin and W. Goddard III, *MRS Symp. Ser.*, 1999, **554**, 43.
- S14. H. Rafii-Tabar and A. S. Sutton, *Phil. Mag. Lett.*, 1991, **63**, 217.
- S15. W. Smith, W. C. Yong and P. M. Rodger, *Molecular Simulations*, 2002, **28**, 86.

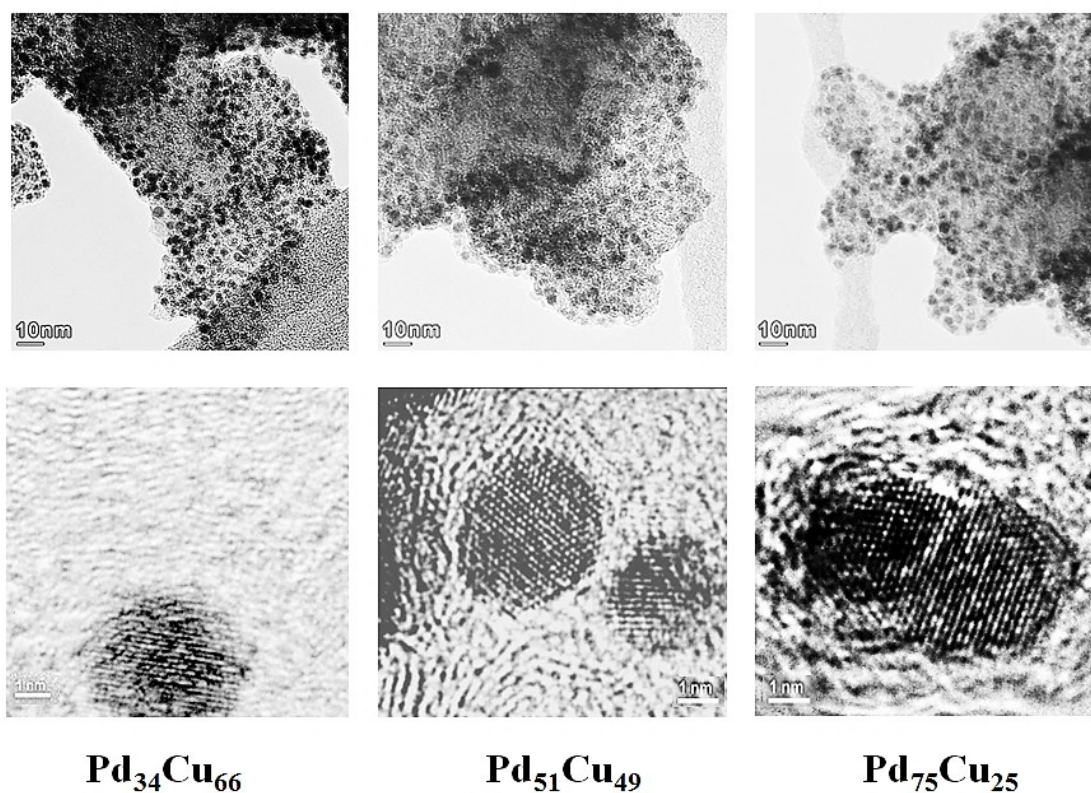


**Figure S1.** Representative TEM (first row) and HR-TEM (second row) images for fresh Pd-Cu NPs. The NPs appear spherical in shape and with an average size of approximately 5.1 ( $\pm$  0.5) nm. Also, the NPs exhibit a good degree of crystallinity, as revealed by the clear lattice fringes appearing in the HR-TEM images. Note, the “ $\pm$ ” deviation from the average NP size is the half width at full maximum of a gaussian-like distribution of sizes extracted from populations of several hundred NPs sampled by different TEM images.

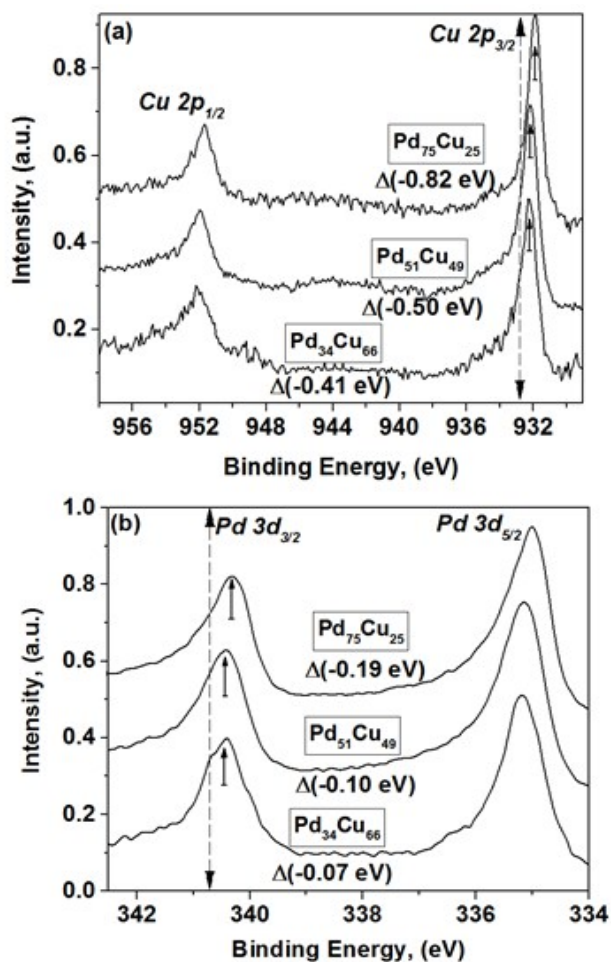


**Figure S2.** Typical XPS (a) Cu  $2p_{3/2}$  and (b) Pd  $3d_{3/2}$  spectra for fresh Pd-Cu NPs. The shift,  $\Delta$ , of the core-level binding energy of Cu and Pd atoms in the respective NPs (vertical arrows pointing upward) are evaluated with respect to the Cu  $2p_{3/2}$  (932.7 eV) and Pd  $3d_{3/2}$  (340.7 eV) lines (vertical arrows pointing downward) characteristic to bulk Cu and Pd metals, respectively.

**Table S1.** Electrochemical active surface area (ECSA), mass activity (MA) and specific activity (SA) for fresh Pd-Cu NPs. Data for pure Pd NPs are also given for comparison.

Catalyst		ECA (m <sup>2</sup> /g <sub>Pd</sub> )	Mass Activity (A/ mg <sub>Pd</sub> )	Specific activity (mA/cm <sup>2</sup> <sub>Pd</sub> )
<b>Pd/C</b>		26	0.17	0.64
<b>PdCu</b>	Pd <sub>25</sub> Cu <sub>75</sub> /C	23	0.014	0.060
	Pd <sub>58</sub> Cu <sub>42</sub> /C	81	0.16	0.20
	Pd <sub>77</sub> Cu <sub>23</sub> /C	101	0.083	0.080

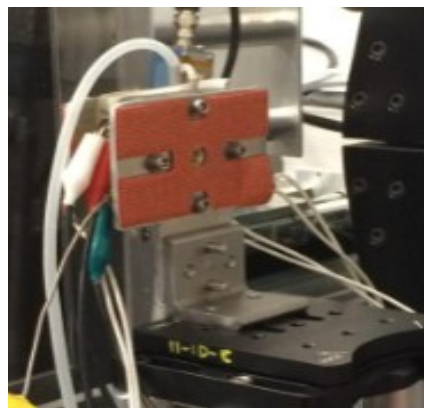
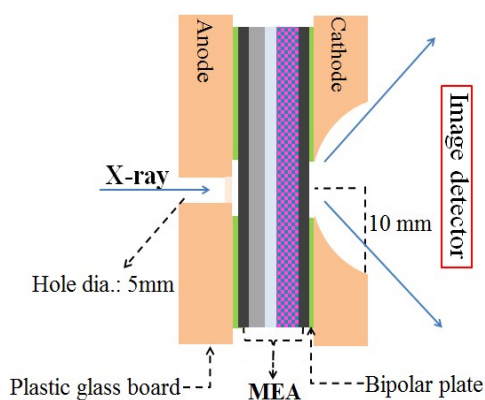


**Figure S3.** (left) Schematic of the custom-built PEMFC used in the present studies. To minimize unwanted x-ray scattering from the PEMFC hardware, holes are drilled through the PEMFC anode and cathode sides down to the sheet of carbon paper (Spectracarb 2050A-0550) used as hydrogen and oxygen diffusion layer, respectively. Thin Kapton foil is used to seal the holes. X-rays enter the PEMFC through the hole in its anode side and leave it through the hole in its cathode side. The latter looks into a large area detector (Perkin Elmer amorphous Si-based flat panel detector) used to collect x-ray intensities scattered from the PEMFC cathode catalyst (right). The PEMFC as used at the beamline 11-ID-C at the Advanced

Photon Source, Argonne. Gas lines and the heater (in brown), used to maintain pre-desired temperature ( $\sim 80$  °C) during the PEMFC operation are clearly visible.

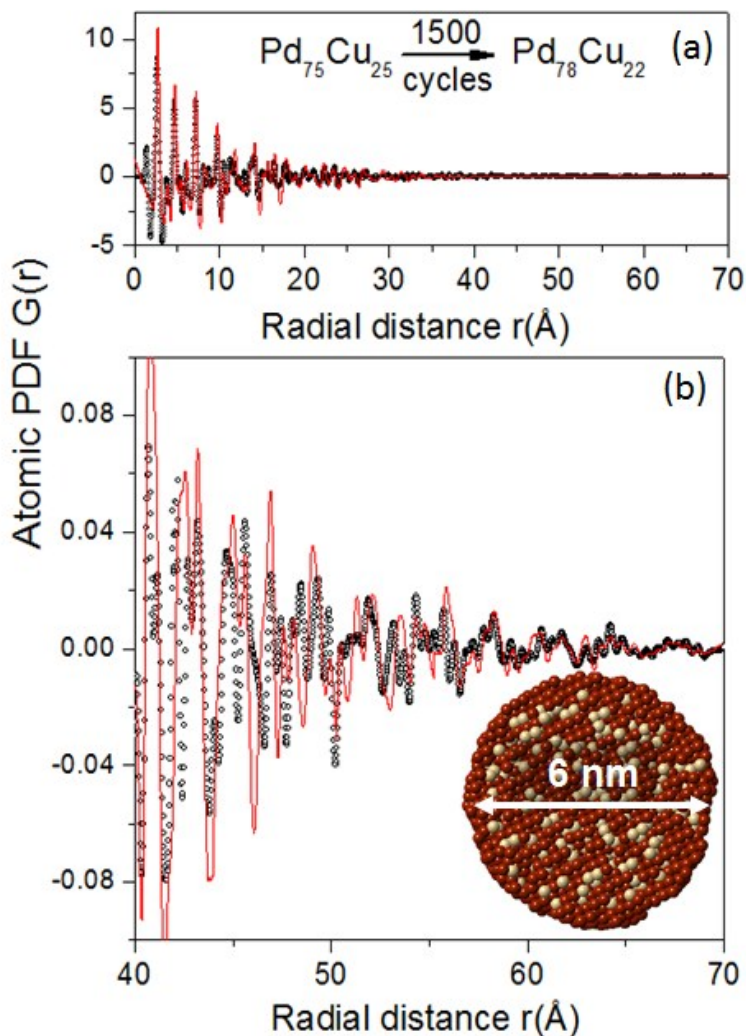


**Figure S4.** (a) Experimental (symbols) and computed (red line) *in operando* atomic PDF for  $\text{Pd}_{75}\text{Cu}_{25}$  alloy NPs undergone 1450 voltage cycles inside the PEMFC shown in Figure S3. The computed PDF is derived from a model nanophase featuring 6 nm fcc Pd-Cu alloy particles rich in Pd at the surface (see Figure S10). For convenience, a cross section of the model is shown in (b). During the cycling, the average size of the NPs has increased from  $5.1(\pm 0.5)$  nm to about  $5.9(\pm 0.5)$ . Hence, both the *in operando* and computed PDF show physical oscillations up to 6 nm. Pd atoms are in red and Cu atoms are in yellow.

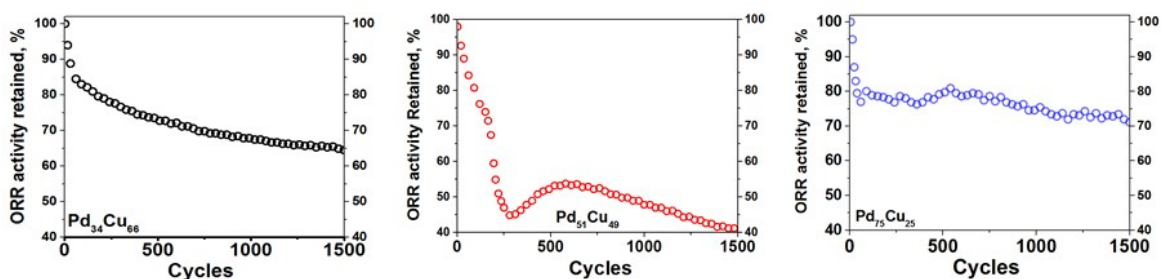


**Figure S5.** Rate of retention (in %) of the effective MA of  $\text{Pd}_x\text{Cu}_{100-x}$  alloy NPs ( $x=34, 51$  and  $75$ ) for ORR during 1450 potential cycles inside the PEMFC. Data reflect the current output of the PEMFC at 0.9 V on the respective polarization curves shown in Figure S15. Note, data are normalized against the MA values for the respective fresh, i.e. not cycled, NPs. Also, note, for legibility purposes, the vertical axis starts from 40%.

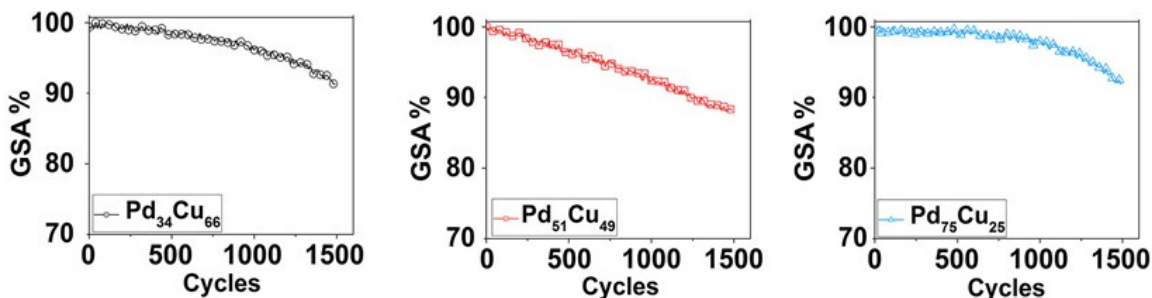


**Figure S6.** Rate of retention (in %) of the GSA of  $\text{Pd}_x\text{Cu}_{100-x}$  alloy NPs ( $x=34, 51$  and  $75$ ) during 1450 potential cycles. The GSA is obtained from the FWHM of the Bragg-like peaks in the respective *in operando* HE-XRD patterns summarized in Figure 1. Note, data are normalized against the GSA, i.e. size, of the respective fresh NPs as determined by independent TEM and HE-XRD experiments described in the text. Also, note, for legibility purposes, the vertical axis starts from 70%.

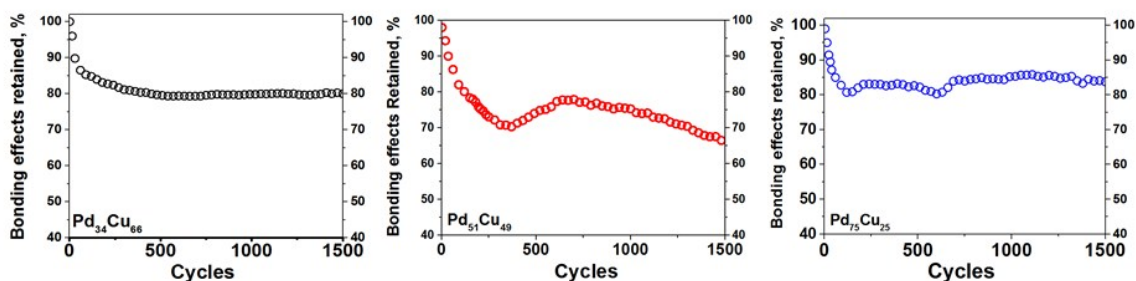


**Figure S7.** Rate of retention (in %) of the bonding effects (geometric and ligand) in Pd<sub>x</sub>Cu<sub>100-x</sub> alloy

NPs ( $x=34, 51$  and  $75$ ) during 1450 pot distances in the respective NPs. The *operando* PDFs summarized in Figure Pd bonding distance in bulk Pd ( $2.76 \text{ \AA}$ ). Hence, as explained in the text, the sma undergone a particular number of cycle effects retained by the NPs. Also, note

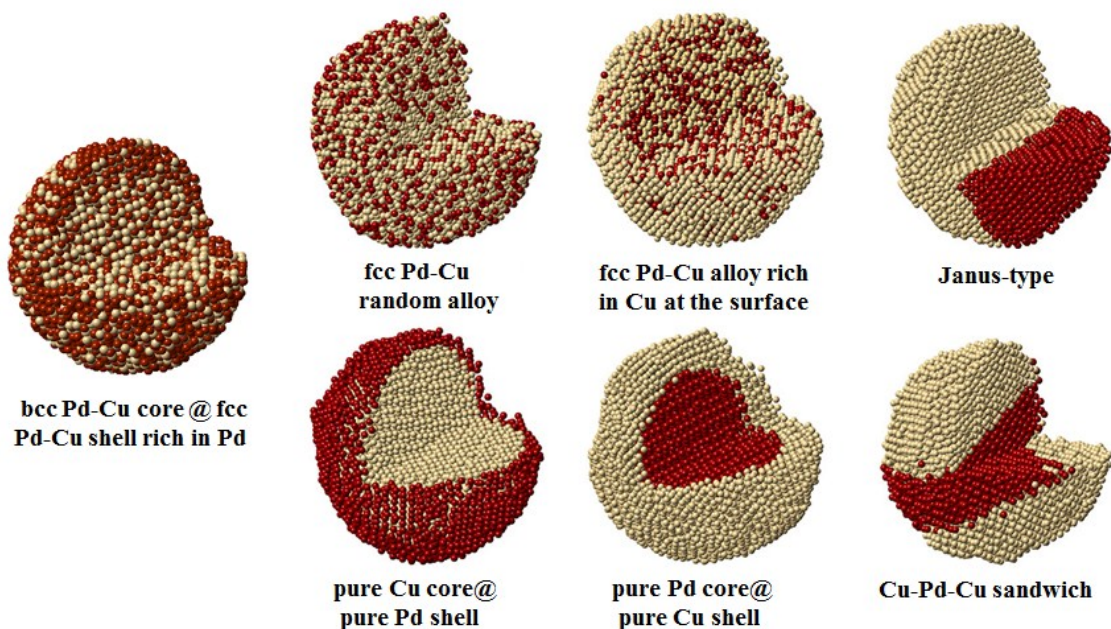


**Figure S8.** MD built plausible nanophases for Pd-Cu alloy NPs with an overall chemical composition of Pd<sub>1</sub>Cu<sub>3</sub> and size of 6 nm. The nanophases feature (from left to right) fcc Pd-Cu random alloy NPs, fcc Pd-Cu alloy NPs whose surface is enriched in Cu, Janus-type Pd-Cu NPs, bcc Pd-Cu alloy core @ fcc Pd-Cu shell NPs whose surface is enriched in Pd, pure Cu core@pure Pd shell NPs, pure Pd core@pure Cu shell NPs and Cu-Pd-Cu sandwich-type NPs. Cu atoms are in yellow and Pd atoms are in red.

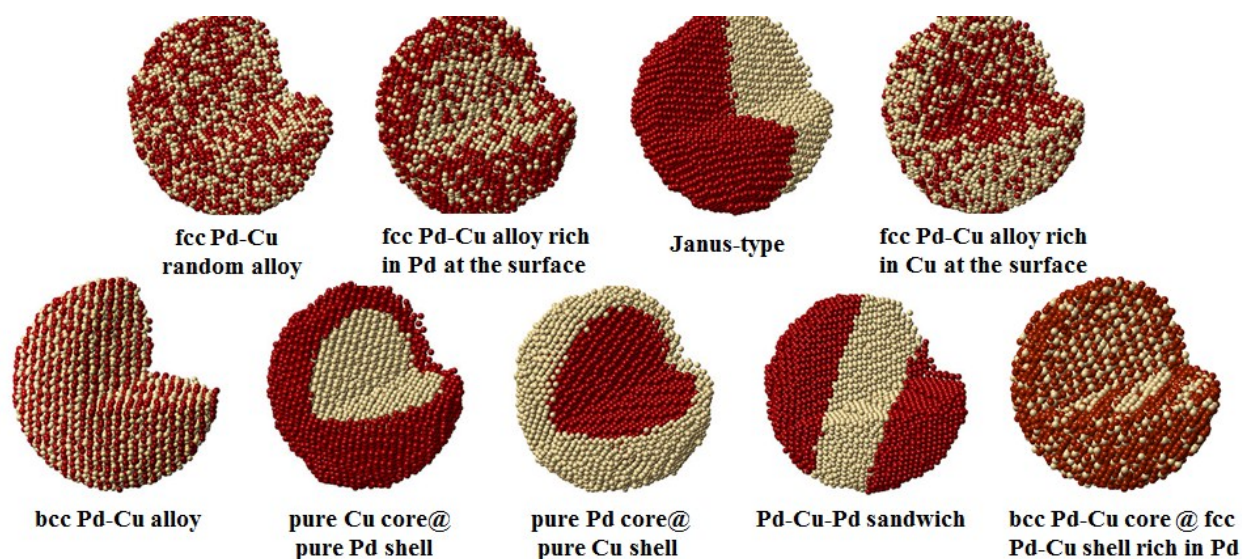


**Figure S9.** MD built plausible nanophases for Pd-Cu alloy NPs with an overall chemical composition of Pd<sub>1</sub>Cu<sub>1</sub> and size of 6 nm. The models feature (from left to right) fcc Pd-Cu random alloy NPs, fcc Pd-Cu alloy NPs whose surface is enriched in Pd, Janus-type Pd-Cu NPs, fcc Pd-Cu alloy NPs whose surface is enriched in Cu, bcc Pd-Cu alloy NPs, pure Cu core@Pd shell NPs, pure Pd core@pure Cu shell NPs, Pd-Cu-Pd sandwich type NPs and bcc Pd-Cu alloy core @ fcc Pd-Cu shell NPs whose surface is enriched in Pd. Cu atoms are in yellow and Pd atoms are in red.

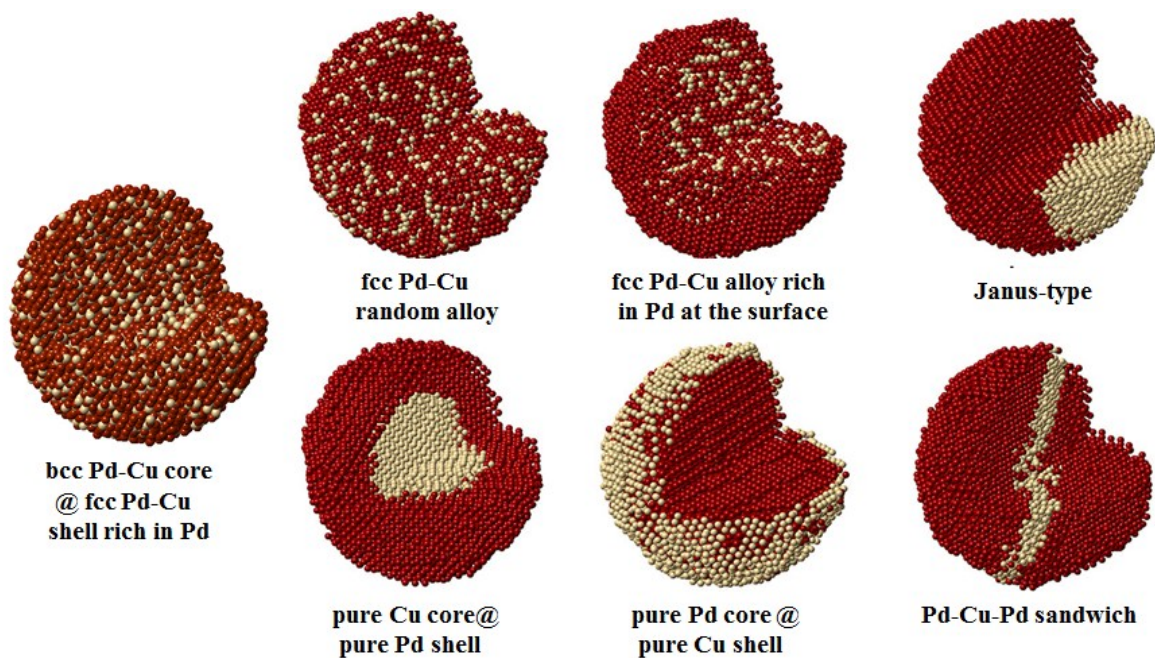


**Figure S10.** MD built plausible nanophases for Pd-Cu alloy NPs with an overall chemical composition of Pd<sub>3</sub>Cu<sub>1</sub> and size of 6 nm. The nanophases feature (from left to right) fcc Pd-Cu random alloy NPs, fcc Pd-Cu alloy NPs whose surface is enriched in Pd, Janus-type Pd-Cu NPs, bcc Pd-Cu alloy core @ fcc Pd-Cu shell NPs whose surface is enriched in Pd, pure Cu core@pure Pd shell NPs, pure Pd core@pure Cu shell NPs and Pd-Cu-Pd sandwich-type NPs. Cu atoms are in yellow and Pd atoms are in red.

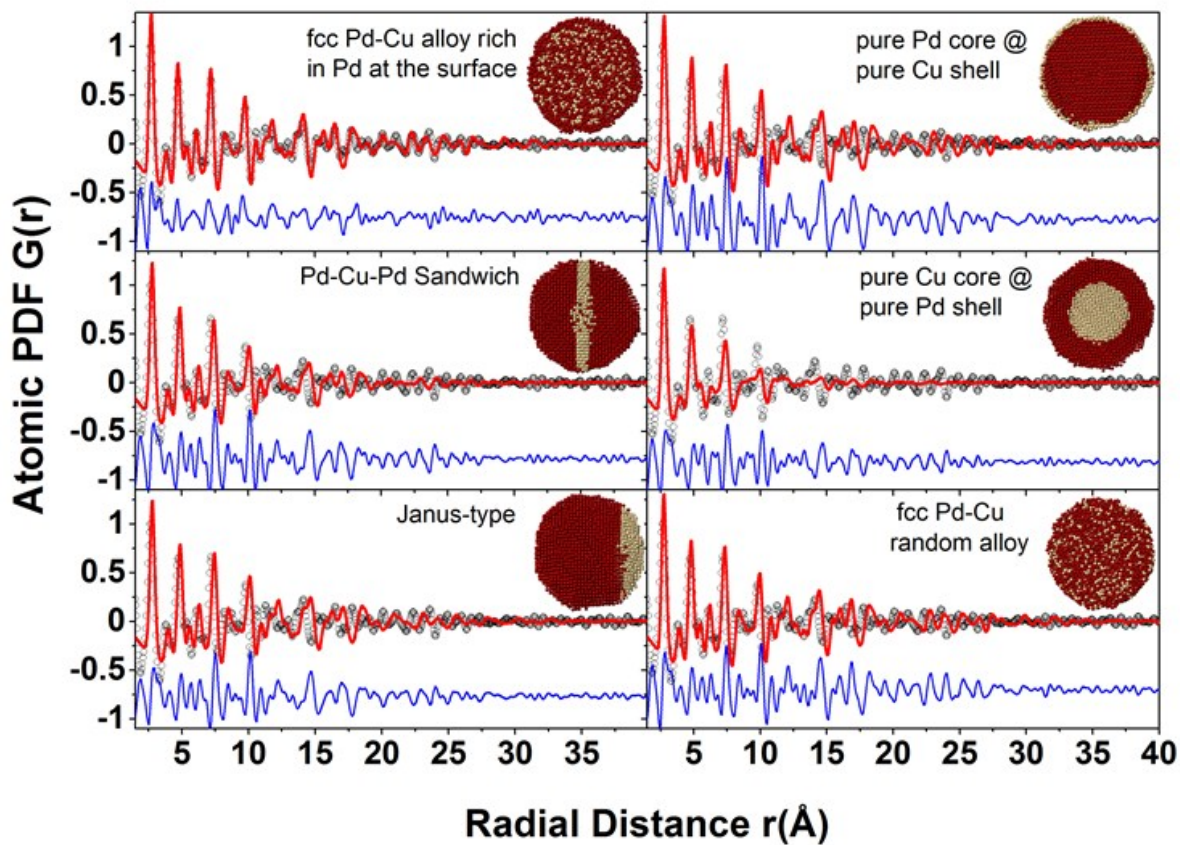


**Figure S11.** Exemplary nanophase analysis for Pd<sub>75</sub>Cu<sub>25</sub> NPs undergone 1450 PEMFC cycles. The difference (blue line) between the experimental (symbols) and model PDFs (red line) derived from the nanophases shown in Figure S9 is shifted by a constant factor for clarity. Snap-shots of the respective nanophases are also given.

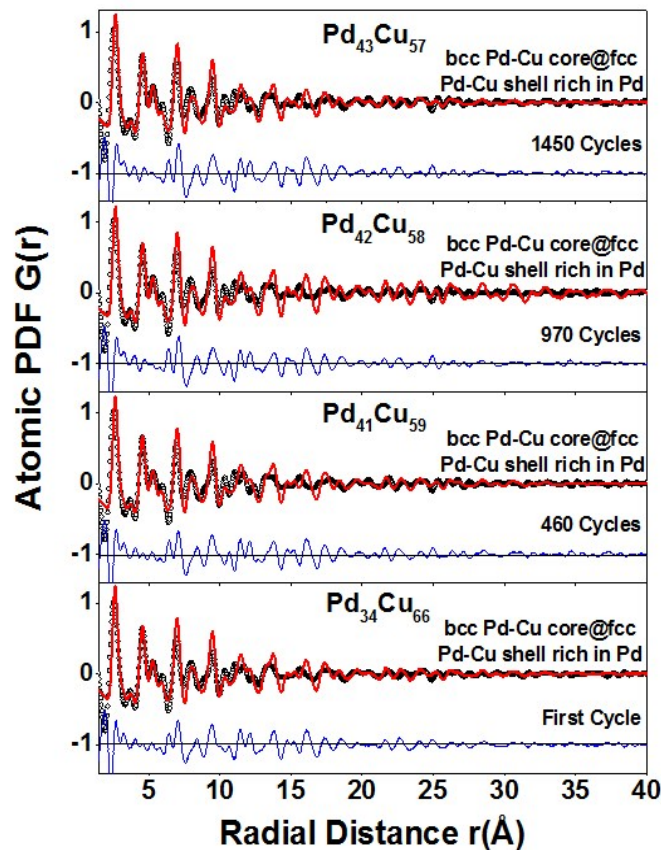


**Figure S12.** Exemplary experimental (symbols) and computed (red line) atomic PDFs for Pd<sub>34</sub>Cu<sub>66</sub> alloy NPs used as an ORR catalyst inside an operating PEMFC. Computed PDFs are derived from a model nanophase featuring NPs whose core and shell are a bcc and fcc Pd-Cu alloy, respectively. Besides, the shell is enriched in Pd. The model nanophase is shown in Figure S8. The difference (blue line) between the experimental and model derived PDF data is shifted by a constant factor for clarity. Note, the chemical composition of fresh (first cycle) and extensively cycled (1450 cycles) NPs was determined by independent ICP-AES experiments.

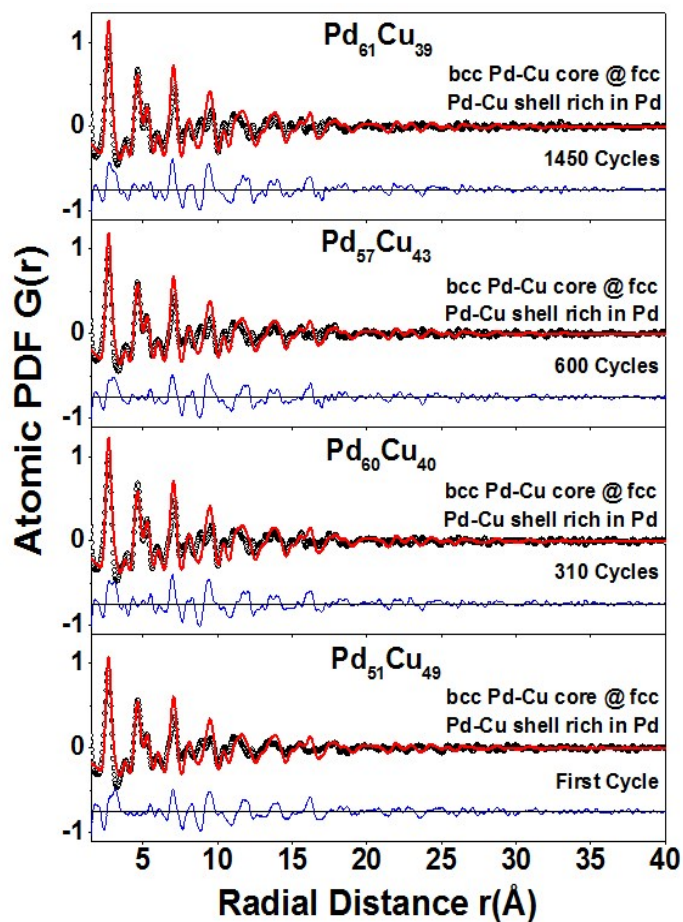


**Figure S13.** Exemplary experimental (symbols) and computed (red line) atomic PDFs for Pd<sub>51</sub>Cu<sub>49</sub> alloy NPs used as an ORR catalyst inside an operating PEMFC. Computed PDFs are derived from a model nanophase featuring NPs whose core and shell are a bcc and fcc Pd-Cu alloy, respectively. Besides, the shell is enriched in Pd. The model nanophase is shown in Figure S9. The difference (blue line) between the experimental and model derived PDF data is shifted by a constant factor for clarity. Note, the chemical composition of fresh (first cycle) and extensively cycled (1450 cycles) NPs was determined by independent ICP-AES experiments.

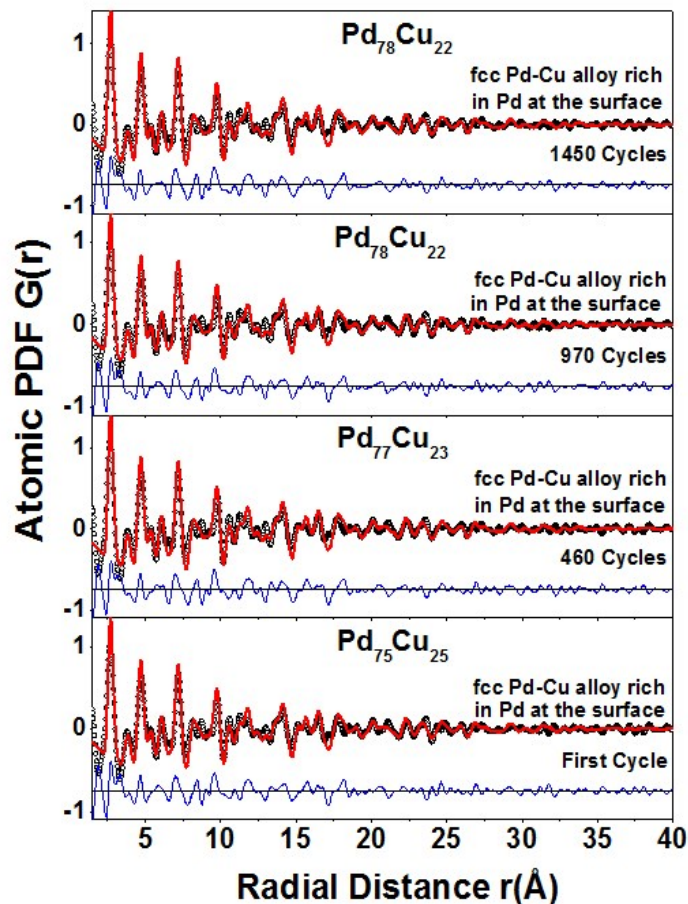


**Figure S14.** Exemplary experimental (symbols) and computed (red line) atomic PDFs for Pd<sub>75</sub>Cu<sub>25</sub> alloy NPs used as an ORR catalyst inside an operating PEMFC. Computed PDFs are derived from a model nanophase featuring an fcc Pd-Cu alloy whose surface is Pd rich. The model nanophase is shown in Figure S10. The difference (blue line) between the experimental and model derived PDF data is shifted by a constant factor for clarity. Note, the chemical composition of fresh (first cycle) and extensively cycled (1450 cycles) NPs was determined by independent ICP-AES experiments.

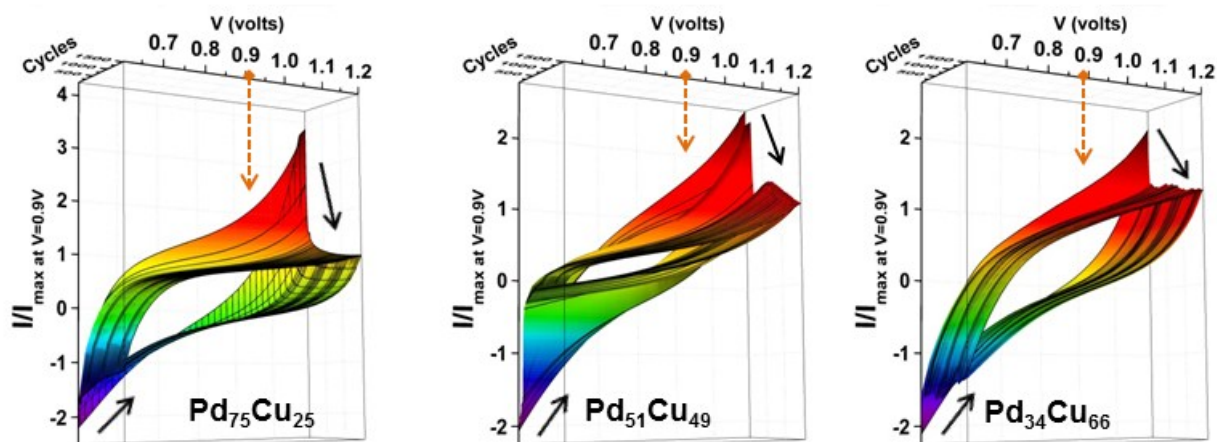
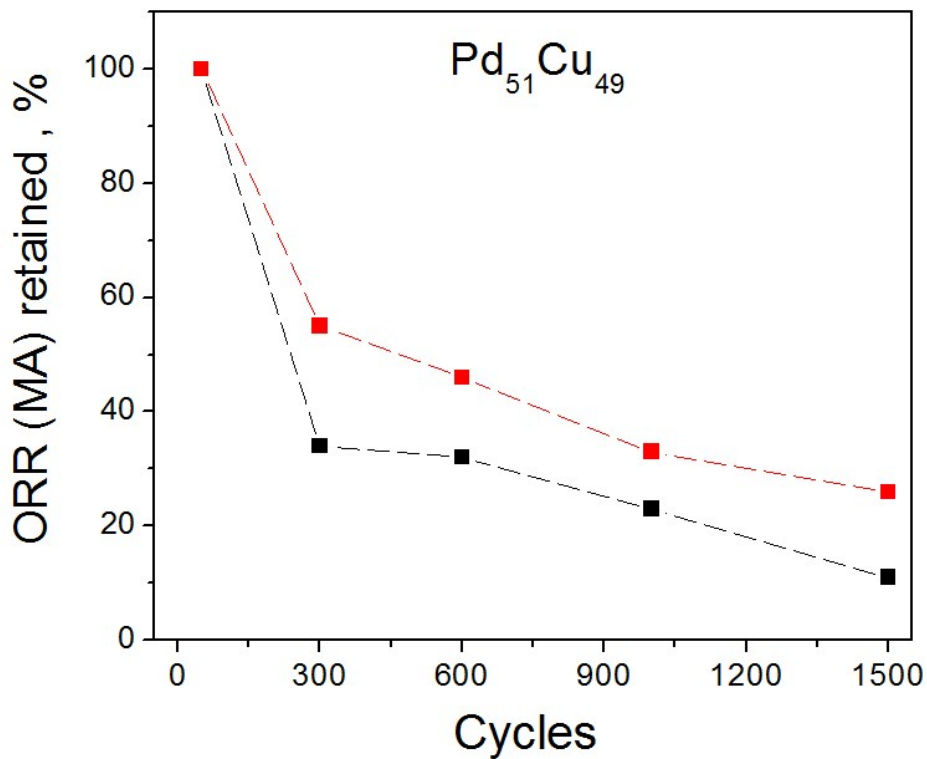
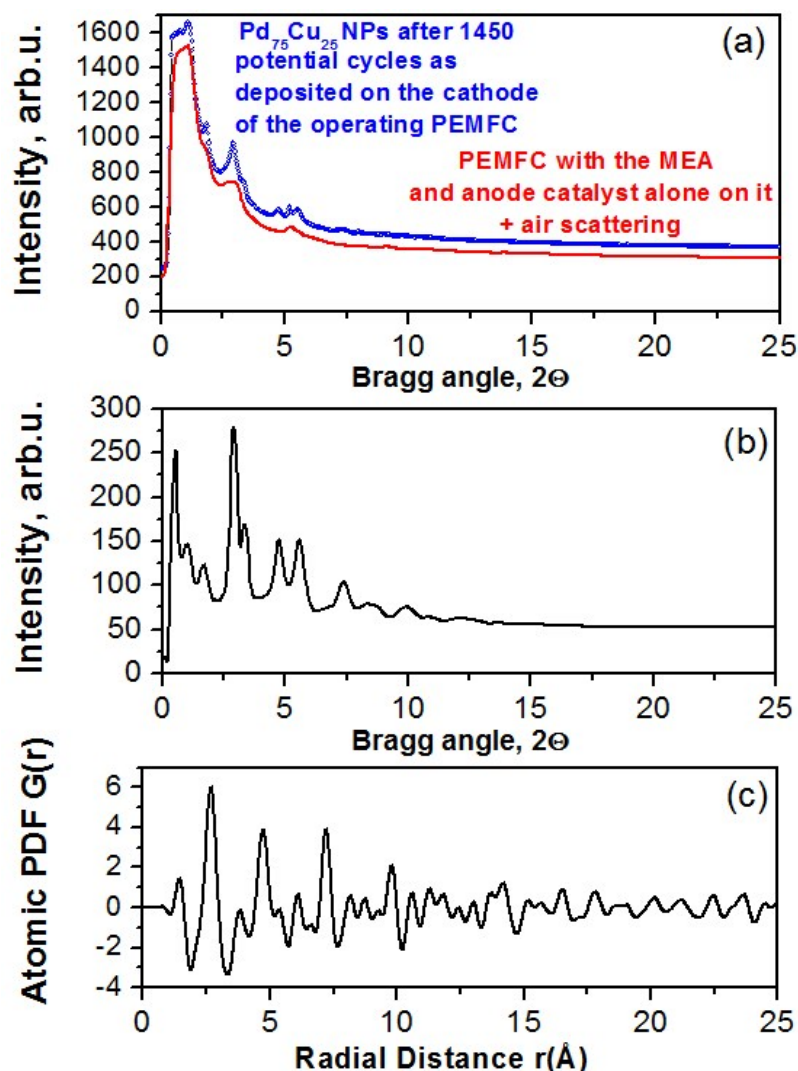


Figure S15. Polarization curves representing the PEMFC current output recorded during 1450 potential cycles in the range from 0.6 V to 1.2 V. The branch of the curves corresponding to “negative” values of the current at voltages close to 0.6 V is given in blue. The color gradually changes to green when the current values approach zero; that is, when the applied external voltage approaches 0.9 V, and vice versa. On the other hand, the branch of the curves corresponding to “positive” values of the current at voltages close to 1.2 V is given in red. The color gradually changes to yellow when the current values approach zero; that is, when the applied external voltage approaches 0.9 V, and vice versa. The curves tend to flatten out with the number of cycles as emphasized by the slanted black arrows. That is because, under actual operating conditions, the ORR activity of the PEMFC cathode catalyst, i.e. Pd-Cu alloy NPs, decays fast. Following the protocol of *ex situ* catalytic studies, the current output of the PEMFC at 0.9 V on the polarization curves (follow the orange vertical arrows) is used as a measure of the effective MA of Pd<sub>x</sub>Cu<sub>100-x</sub> NPs (x=34, 51 and 75) for ORR taking place at the cathode of an operating PEMFC. The so obtained MA values are summarized in Figure S5.



**Figure S16.** Rate of retention (in %) of the MA of Pd<sub>51</sub>Cu<sub>49</sub> NPs for ORR during 1500 potential cycles between 0.6-1.2 V (vs. RHE) in N<sub>2</sub>-saturated 0.1 M HClO<sub>4</sub> solution. The respective MA values are determined by measuring the kinetic current of an RDE curve at 0.8 V vs. RHE in O<sub>2</sub>-saturated 0.1 M HClO<sub>4</sub> solution. Data in red and black reflect results of two independent tests.



**Figure S17.** (a) XRD pattern for Pd<sub>75</sub>Cu<sub>25</sub> NPs undergone 1450 potential cycles (blue symbols) taken when the sample is at the cathode of the operating PEMFC. Background-type scattering originating from the PEMFC hardware, including the MEA with the anode (pure Pt) catalyst alone deposited on it, and air surrounding the PEMFC is also shown (red line). Note, the “bumps” in the background-type scattering seen at about  $2\theta=2.5$  and  $2\theta=5$  degs. come from the graphitic paper used in MEAs. Scattering from the anode catalyst is hardly seen because, typically, actual PEMFCs do not require a large amount of anode catalysts to operate. The rapid increase in the scattered x-ray intensities below  $2\theta=2.5$  degs. is due to strong air scattering close to the center/position of the synchrotron x-ray beam. X-ray data below  $2\theta=2.5$  degs. though are not used in the present studies because the XRD patterns of Pd-Cu NPs do not show physical features at such low Bragg angles. (b) XRD pattern from (a) as corrected for the “background-type” scattering shown in (a). The pattern is dominated by diffraction features originating from the PEMFC cathode catalyst. (c) Atomic PDF derived from the XRD pattern shown in (b). Features of the PDF are discussed in the paper (see Figure 2b and the related to it text).